

Multipolar plasmon resonances in supported silver particles: The case of Ag/ α -Al₂O₃(0001)

Rémi Lazzari,^{1,2,*} Stéphane Roux,^{1,†} Ingve Simonsen,^{1,3,‡} Jacques Jupille,^{1,§} Dick Bedeaux,^{4,||} and Jan Vlieger⁴

¹Laboratoire Mixte CNRS/Saint-Gobain (UMR 125) "Surface du Verre et Interfaces,"

39, Quai Lucien Lefranc, BP 135, F-93303 Aubervilliers Cedex, France

²CEA Grenoble, Département de Recherche Fondamentale sur la Matière Condensée, Service de Physique des Matériaux et Microstructures-Interfaces et Rayonnement Synchrotron, 17, Rue des Martyrs, F-38054 Grenoble Cedex 9, France

³Department of Physics, Theoretical Physics Group, The Norwegian University of Science and Technology (NTNU), N-7034 Trondheim, Norway

⁴Leiden Institute of Chemistry, Leiden University, P.O. Box 9502, 2300 RA Leiden, The Netherlands

(Received 26 February 2002; published 10 June 2002)

The present paper is devoted to the description of optical absorptions in supported metallic particles smaller than the wavelength of light. The breaking of symmetry brought by the presence of the substrate and by the finite contact angle for the particle leads to a nonhomogeneous local field and allows excitation of multipolar absorption modes. Their energetic positions, oscillator strengths, and widths are calculated in the limit of zero damping by use of a multipolar expansion of the potential inside and around the island. The charge vibration pattern and the location of the field enhancements are clearly identified for each mode. Even if the dipolar mode is the most intense, the highlighting of the secondary modes in optical measurements is possible in peculiar experimental conditions. Some experiments of surface differential reflectivity spectroscopy for silver deposits on oxide substrates are given as examples.

DOI: 10.1103/PhysRevB.65.235424

PACS number(s): 78.20.Bh, 61.46.+w, 68.55.Ac, 73.20.Mf

I. INTRODUCTION

Over the last 100 years, there has been a tremendous theoretical and experimental work on the optical properties of metallic particles¹ as they represent an intermediate state between molecules and solid. The starting point was the work of Maxwell Garnett² at the turn of the century. He gave the first explanation of the coloration of glasses doped by a metal precursor. The link between the optical properties of such glasses and the presence of metallic particles was not obvious since the bulk dielectric constant of metal does not show such absorptions. A more complete derivation of light scattering by a spherical particle was given by Mie in 1908.³ He solved the complete Maxwell equations for an incoming plane wave on a sphere by the method of Rayleigh partial waves and calculated the scattering and absorption cross sections. Of course, in the size regime where the particle radius is much smaller than the wavelength of light ($x=R/\lambda < \text{few } \%$), the quasistatic approximation can be assumed by solving only the Laplace equation for the potential. In this case, the main effect of the electric field is to polarize the electronic gas of the metal and to excite collective motion of electrons: surface plasmon polaritons. The term surface finds its origin in the fact that, despite a collective oscillation of the electronic gas with respect to the positive background of ions in a jellium picture, the restoring force comes from the surface polarization. The excited quasiparticles are a result of the mixing of plasmon and photons. In dielectric particles, exactly the same phenomenon occurs in the infrared with excitation of phonons (surface phonon polaritons). For a metallic sphere, the polarization process leads simply to a dipole behavior with a surface charge distribution equal to the cosine of the angle between the homogeneous exciting electric field and the current point on the surface. In the quasistatic size regime, the extinction cross section σ_{ext} is mainly given by absorption σ_{abs} as the scattering σ_{sca}

$\sim (R/\lambda)^4$ is of three orders of magnitude lower than absorption $\sigma_{abs} \sim (R/\lambda)$. More precisely one has:

$$\sigma_{ext} = 9 \frac{\omega}{c} \epsilon_m^{3/2} V_0 \frac{\epsilon_2(\omega)}{[\epsilon_1(\omega) + 2\epsilon_m]^2 + \epsilon_2(\omega)^2}, \quad (1)$$

where $\epsilon(\omega) = \epsilon_1(\omega) + i\epsilon_2(\omega)$ is the frequency-dependent dielectric constant of the metal particle, ϵ_m the dielectric function of the surrounding medium, and $V_0 = (4\pi/3)R^3$ the volume of the cluster. A resonance occurs at the minimum of the denominator $[\epsilon_1(\omega) + 2\epsilon_m]^2 + \epsilon_2(\omega)^2$. If $\epsilon_2(\omega)$ is small or does not vary in the considered frequency region, one recovers the classical relation $\epsilon_1 = -2\epsilon_m$ for the Fröhlich mode of a sphere. With a Drude metal, the absorption is found at $\omega = \omega_p/\sqrt{3}$ with ω_p the bulk plasmon frequency. For an ellipsoidal particle, the same type of dipolar vibrations are seen along the main axis. However, by breaking the symmetry of the surrounding, high-order multipoles can be excited.

The first example is when the ratio between the sphere radius and the wavelength increases. For such particles sizes, the incoming field E_0 develops oscillations inside the particle in such a way that neglecting the retardation effects becomes not valid. The nonhomogeneous field E_0 allows the appearance of electric and magnetic multipoles. Far away from the cluster, the associated waves are identical to those coming from equivalent point multipoles. As underlined above, the electric multipolar modes are linked to surface polarization while magnetic multipoles are due to eddy currents. Clear experimental evidence of these modes is scarce in the literature.^{4,5} The great difficulty in experimental spectra is to overcome the size distribution of the particle collection and the interface damping^{6,7} which smear out all the structures. Moreover, the mixing between absorption and scattering modes implies the use of many experimental techniques to be separated. Most of the time, noble metals like silver or alkali are chosen for their free-electron gas behavior. Their

plasma oscillations are not damped by interband transitions and the absorption structures are sharp.

Another way to put forward this phenomenon is to study irregularly shaped particles. In this case, the inhomogeneity does not come from the exciting field but from the particle susceptibility itself. Even in the quasistatic regime, a great variety of charge vibration patterns can be excited particularly in the presence of sharp corners. These type of geometries are encountered in the faceting processes of nanocrystallites. The Wulff construction at thermodynamic equilibrium⁸ gives the relative spreads of the crystallographic planes and the overall crystal shape. Fuchs⁹ tried to illustrate this phenomenon by computing the phonon-polariton absorptions of small dielectric cubes like NaCl or MgO. He underlined the importance of corners in the trapping of polarization charges. Furthermore, optical studies are often performed on supported particles. Their final shape arises from a complex balance between thermodynamic and kinetics factors but, at least, the notion of contact angle has to be introduced to describe the geometry of the system and the wetting properties. The influence on the optical absorptions of such a line of contact between three dielectric media is poorly known. Moreover, the presence of the substrate complicates greatly the situation as it brings a new breaking of symmetry with the image field, even for a supported sphere.^{10,11} In the quasistatic regime, the optical behavior of a particle on a substrate can be seen as a cascade of polarization processes. The incident field creates a dipole inside the particle. The substrate reacts by creating an image dipole which in turn modifies the local field around the island. This image dipolar field excites the quadrupolar polarizability of the island and as a consequence a quadrupole image appears in the substrate and so on. This mechanism of image interaction is in a complicated way linked to the multipolar polarizabilities of the particle. But even if Beita *et al.*¹² and Chauvaux and Meesen¹³ detected and underlined this phenomenon on supported alkali clusters, clear evidence of such multipolar absorptions is still lacking because of experimental difficulties and because rather crude simple models are often used to interpret the optical response of supported particles.^{14–16}

The aim of the present paper is to demonstrate the occurrence of multipolar absorption modes in experimental spectra from small supported particles and to give a description of these modes in the nonretarded limit for supported truncated spherical particles. The paper is organized as follows. After a description of the experimental setup in Sec. II, surface differential reflectivity (SDR) spectra from silver nanoparticles supported by alumina substrates are presented in Sec. III. In the discussion of Sec. IV, it is explained that the multipolar modes are found in the zero damping limit. The role of substrate in their appearance and of the way to reveal them by increasing the coupling between the particles are studied. Oscillator strengths and broadenings of these modes are evaluated to first order in the imaginary part of the dielectric constant. The model is then applied in Sec. V to the experiments of *in situ* SDR for silver on alumina. Clear evidence is given of the occurrence of multipolar modes.

II. EXPERIMENTAL SETUP

Experiments have been performed in a ultra high-vacuum chamber equipped with the classical surface science tools (base pressure 3×10^{-8} Pa). The sapphire α -Al₂O₃(0001) samples purchased from Matek GmbH were epitaxially polished with a miscut less than 0.2° as checked by *ex situ* atomic force microscopy. Once mounted on a tantalum plate in UHV, thanks to an electronic bombardment system, the substrates were cleaned by a strong annealing under partial oxygen pressure provided by a gas dosing pipe.¹⁷ The surface composition was checked by x-ray photoemission and the C 1s line was below the detection limit. This procedure allows us to obtain a (1×1) sharp low-energy electron diffraction (LEED) pattern. Silver was evaporated from a Knudsen cell and the flux calibrated by a quartz microbalance (0.07 ML/s with 1 ML given by the spacing between two atomic plane along the [111] direction of the fcc structure). The sample temperature was regulated at $T=600$ K by a Chromel-Alumel thermocouple force wedged to the substrate surface.

The optical experiment used to monitor *in situ* and in real time the growth is surface differential reflectivity spectroscopy. The recorded quantity is the relative variation of the sample reflectivity:

$$\frac{\Delta R}{R} = \frac{R - R_0}{R_0}. \quad (2)$$

The reference is the reflectivity of the bare substrate, R_0 . The light emitted by a deuterium lamp in the UV-visible range (1.5–6 eV) is collimated on the sample with an incident angle of 45°, collected in *p* or *s* polarization and dispersed by a grating spectrograph (300 grooves/mm) on a Peltier-cooled photodiode array. The environment is carefully controlled during the recording of the optical spectra. This advice is of course essential with highly reactive metals like alkali.^{18–20} But more generally, the surface plasmon even with noble metal is highly sensitive to the adsorbed species. The phenomenon of interface damping put forward by Kreibig and co-workers and Personn^{6,7,21} induces a strong broadening of the absorptions peaks. Thus, it is really difficult to identify the multipolar resonances for sample submitted to ambient atmosphere or elaborated by a chemical way.

It is well known that the low affinity of noble metal with dielectric substrates leads to a cluster growth mode²² with typical size in the nanometric range. Upon deposition, the morphology of the thin film is dictated by both thermodynamics and kinetics factors, leading in most situations to a broad distribution of clusters shapes and sizes^{22,23} (from 20% to 100%) which mixes up all the features. The substrate inhomogeneities worsen the situation by creating nucleation centers and paths of diffusion of different energies. The way to reduce the width of the distribution up to a few tens of a percent is to activate the diffusion process and to get closer to the thermodynamic equilibrium by increasing the temperature. Thus, in the present case, the sample temperature was regulated at $T=600$ K.

III. REFLECTIVITY OF SILVER THIN FILMS

SDR spectra collected during the deposition of silver on α -Al₂O₃(0001) are shown in Fig. 1. Spectra collected in *p*

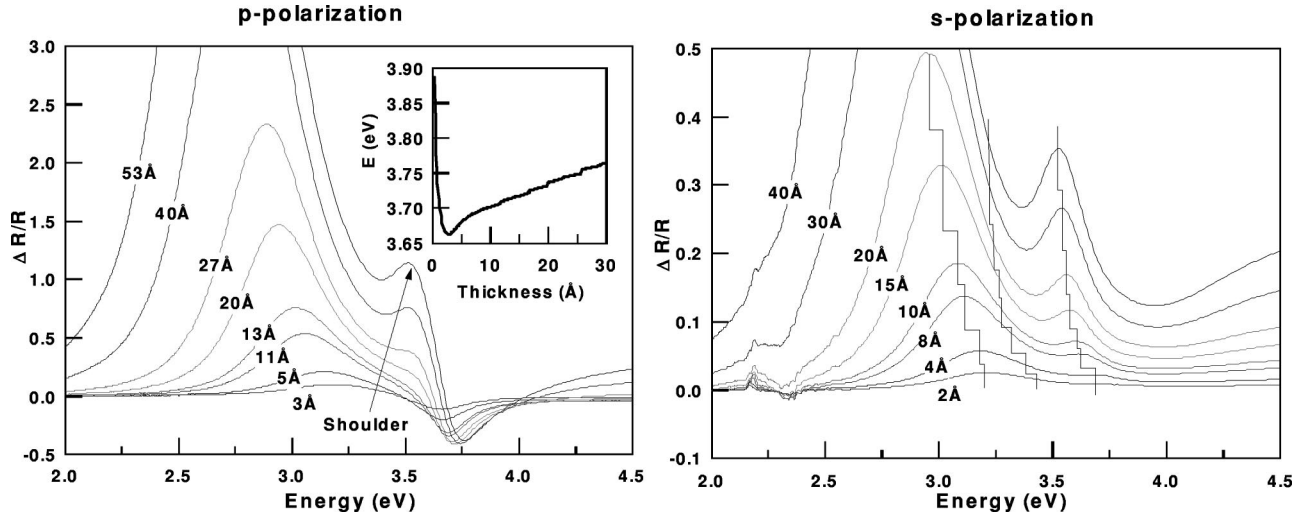


FIG. 1. Evolution of the SDR spectra recorded during the growth of a thin silver film at $T=600$ K on $\text{Al}_2\text{O}_3(0001)$ in p (left panel) or s (right panel) polarization. The dispersion of the high-energy resonance with deposited thickness for the p polarization is given in the inset. The evolution of the main structures in s polarization is displayed with broken lines to guide the eye.

polarization involve three features lying above 3.6 eV, around 3.5 eV, and below 3.2 eV, respectively. The disappearance of the 3.6-eV peak in s polarization indicates that it is dominated by excitations normal to the surface. At variance, the other features mostly come from excitations parallel to the surface. The positions and shapes of the 3.65–3.9 eV and 3.2–2.6 eV peaks are characteristic of a three-dimensional growth mode.^{24,25}

Redshifted at the beginning of the silver deposition, the high-energy feature of the SDR spectra shifts toward higher energy at a coverage higher than 0.3 nm [inset of Fig. 1(a)]. It is after the onset of this blueshift that the 3.5-eV feature becomes sizable in both polarizations. The two main surface plasmon-polariton peaks in p polarization and the main feature in s polarization are qualitatively understood in the framework of the dipole model^{14,15} and can be modeled by means of multipolar approaches.^{24,25} However, the origin and behavior of the shoulder are to be explained.

IV. DISCUSSION

Because the two main features observed in absorption spectra are assigned to dipolar resonances, the new modes lying around 3.5 eV can be suggested to arise from a multipolar response. In addition, since these modes appear at the onset of the blueshift of the high-energy resonance, they are likely perturbed by particle-particle interactions. A first goal in this discussion is therefore to show how multipolar modes can be identified in the zero-damping limit.

A. Revealing the multipolar modes

The thin film is modeled by a distribution of particles which are represented by truncated spheres (medium 3) supported on a substrate (medium 2), embedded in a medium 1, and excited by a uniform field \mathbf{E}_0 . The buried part of the sphere is introduced as a different medium 4. The corresponding frequency- ω -dependent dielectric functions are de-

noted ϵ_i with $i=1,2,3,4$ ($\epsilon_4=\epsilon_2$). The supported sphere is defined by means of a truncation parameter t_r . The Appendix A presents a detailed derivation of the polarization process of such particles through a multipolar expansion of the potential. The polarizability tensor results from the solution of a linear system of equations for the multipolar coefficients.

For particles smaller than the wavelength, the absorption cross section σ_{abs} is mainly given by the imaginary part of the particle polarizability $\text{Im}(\alpha_m)$ ($m=0, \pm 1$).¹ As for a free sphere in vacuum [see Eq. (1)], the multipolar absorptions are defined by the poles of the polarizabilities in the zero-damping limit which is found when the imaginary parts of the dielectric constants of the particle and the substrate vanish, that is to say $\epsilon_i = \epsilon_i^R + i\kappa\epsilon_i^I$ with $\kappa \rightarrow 0$. To be clearer, let us introduce the following notation for the linear system, Eq. (A5):

$$\mathcal{M}(\omega, \kappa)X(\omega, \kappa) = E(\omega, \kappa). \quad (3)$$

The matrices are denoted by script letters, the vector by italic letters, and the index $m=0, \pm 1$ is most of the time dropped. $\mathcal{M}(\omega, \kappa)$ stands for matrix (A8) which describes the frequency-dependent response of the system up to multipolar order M . Here $X(\omega, \kappa)$ is the vector for the multipolar components of the potential expansion: $X_{lm}(\omega, \kappa) = (A_{lm}, B_{lm})$ with $l=1, \dots, 2M$. The source field which excites the system either parallel $m = \pm 1$ or normal to the surface $m=0$ is $E(\omega, \kappa)$. Thus, as formally,

$$\alpha_m \sim A_{1m} = X_{1m} = [\mathcal{M}(\omega, \kappa)]_{1,l,m}^{-1} E_{l,m}(\omega, \kappa), \quad (4)$$

the resonances occur at frequencies where the matrix $\mathcal{M}(\omega, \kappa)$ eigenvalue finds its lowest moduli. In the zero-damping limit $\kappa \rightarrow 0$, it corresponds to frequencies where these eigenvalues are zero. Another way to understand these resonant modes is to see them as undamped oscillations of the potential which need no external field to be

maintained, which corresponds to $\mathcal{M}(\omega, \kappa=0)\tilde{X}=0$; the solution is found when the determinant of the matrix, $\text{Det}[\mathcal{M}(\omega, \kappa=0)]$, is zero. This condition gives the resonant frequencies ω_r and the associated eigenvectors $\tilde{X}(\omega = \omega_r)$ and matrix $\mathcal{M}(\omega = \omega_r, \kappa=0)$. The corresponding map of the potential gives information on the self-polarization charges since the equipotential lines surround charges.

The oscillator strengths (the integrated intensities) and broadenings of the absorption modes are determined by introducing the damping in the exciting field at resonance $E(\omega = \omega_r, \kappa=0)$ via a limited development of the matrix and of the vector around the point $(\omega = \omega_r, \kappa=0)$ up to first order in the difference $\omega - \omega_r$ and in the damping κ :

$$\mathcal{M}(\omega, \kappa) = \mathcal{M}(\omega_r, 0) + \left(\frac{\partial \mathcal{M}}{\partial \omega} \right) (\omega - \omega_r) + i \left(\frac{\partial \mathcal{M}}{\partial \kappa} \right) \kappa, \quad (5)$$

$$X(\omega, \kappa) = x \tilde{X}(\omega_r) + \left(\frac{\partial X}{\partial \omega} \right) (\omega - \omega_r) + i \left(\frac{\partial X}{\partial \kappa} \right) \kappa. \quad (6)$$

Partial derivatives are taken at $\omega = \omega_r, \kappa=0$. By using $\mathcal{M}(\omega_r, 0)\tilde{X}(\omega_r) = 0$, the linear system, Eq. (3), becomes to first order in κ and $\omega - \omega_r$:

$$\begin{aligned} \mathcal{M}(\omega_r, 0) \left[\left(\frac{\partial X}{\partial \omega} \right) (\omega - \omega_r) + i \left(\frac{\partial X}{\partial \kappa} \right) \kappa \right] \\ + x \left[\left(\frac{\partial \mathcal{M}}{\partial \omega} \right) (\omega - \omega_r) + i \left(\frac{\partial \mathcal{M}}{\partial \kappa} \right) \kappa \right] \tilde{X}(\omega_r) = E(\omega_r, 0). \end{aligned} \quad (7)$$

To determine the amplitude term x , the rotation terms for the eigenvector are eliminated by multiplying this equation by the left eigenvector ${}^t\tilde{Y}(\omega_r)$ of $\mathcal{M}(\omega_r, 0)$. Indeed, as $\mathcal{M}(\omega_r, 0)$, whose determinant is zero, is nonsymmetric, the left $\tilde{X}(\omega_r)$ and right $\tilde{Y}(\omega_r)$ eigenvectors defined by

$$\mathcal{M}(\omega_r, 0)\tilde{X}(\omega_r) = 0, \quad {}^t\mathcal{M}(\omega_r, 0)\tilde{Y}(\omega_r) = 0 \quad (8)$$

are not equal. Thus, one has

$$x = \frac{{}^t\tilde{Y}(\omega_r)E(\omega_r, 0)}{{}^t\tilde{Y}(\omega_r) \left[\left(\frac{\partial \mathcal{M}}{\partial \omega} \right) (\omega - \omega_r) + i \left(\frac{\partial \mathcal{M}}{\partial \kappa} \right) \kappa \right] \tilde{X}(\omega_r)}. \quad (9)$$

Finally, the polarizability is found by multiplying this amplitude x by the first term of the right eigenvector $\tilde{X}(\omega_r)$ in the basis of (A_{lm}, B_{lm}) [Eqs. (A6) and (A7)]. At the limit of small damping by summing on all modes, the polarizability is written in the spectral representation:

$$\alpha = \sum_r \frac{F_r}{\omega_r - \omega - i\gamma_r} + \alpha_0(\omega, \kappa), \quad (10)$$

where F_r and γ_r are the oscillator strength and the width of the absorption peak, respectively:

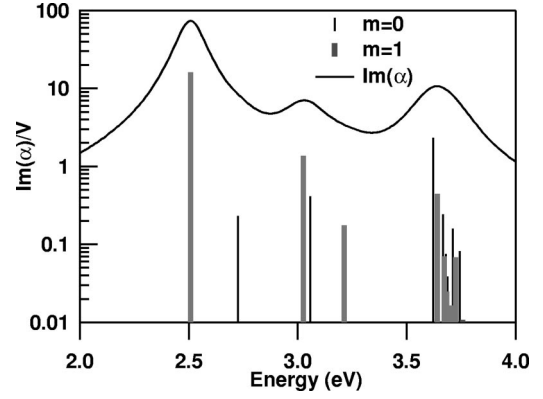


FIG. 2. Absorption peaks defined by the imaginary part of the polarizability normalized by the particle volume $\text{Im}(\alpha_{||} + \alpha_{\perp})/V$ [Eq. (A17)] for a silver hemisphere ($t_r=0$, $M=28$, $\epsilon_2=3$).

$$\begin{aligned} F_r = - \frac{1}{E_0^{inc}} \frac{\tilde{X}_i^r \left(\sum_j E_j \cdot \tilde{Y}_j^r \right)}{\sum_{ij} \tilde{Y}_i^r \left(\frac{\partial \mathcal{M}}{\partial \omega} \Big|_{\omega_r, \kappa=0} \right)_{ij} \tilde{X}_j^r}, \\ \gamma_r = \frac{\kappa \sum_{ij} \tilde{Y}_i^r \left(\frac{\partial \mathcal{M}}{\partial \kappa} \Big|_{\omega_r, \kappa=0} \right)_{ij} \tilde{X}_j^r}{\sum_{ij} \tilde{Y}_i^r \left(\frac{\partial \mathcal{M}}{\partial \omega} \Big|_{\omega_r, \kappa=0} \right)_{ij} \tilde{X}_i^r}, \end{aligned} \quad (11)$$

with $1/E_0^{inc}$ the right normalization by the incident electric field E_0 as given by Eqs. (A6) and (A7). The term $\alpha_0(\omega, \kappa)$ stands for the difference between the approximated spectral representation [sum in Eq. (10)] and the exact polarizability computed by solving the linear system, Eq. (3). A discussion on the validity of such a spectral decomposition is given in the Appendix and the numerical implementation of the problem is presented in the Appendix.

B. Nature of the modes

The oscillator strength and energy of a series of surface plasmon-polariton modes are shown in Fig. 2 in the case of a hemispherical particle of silver supported on a substrate with a dielectric constant $\epsilon_2=3$ which is supposed to be nonabsorbing. The bulk dielectric constant of silver is extracted from Palik's compilation.²⁶ The equipotential lines associated with the four more intense normal and parallel modes are represented in Figs. 3 and 4, respectively. Bearing in mind that the equipotential lines surround the polarization charges, these maps give a visualization of the charge location. The two dipolar modes, which are labeled 0-A and 1-A in Figs. 3 and 4, dominate the optical response. Their oscillator strengths F_r are one order of magnitude greater than the other modes of similar polarization. The (1-A) mode presents a strong pinning of the charge at the triple-contact line between vacuum, substrate, and island, which can be understood in terms of the tip effect in electrostatics. The (0-A) mode corresponds to a dipole with a accumulation of charges at the interface with the substrate and the top of the cluster.

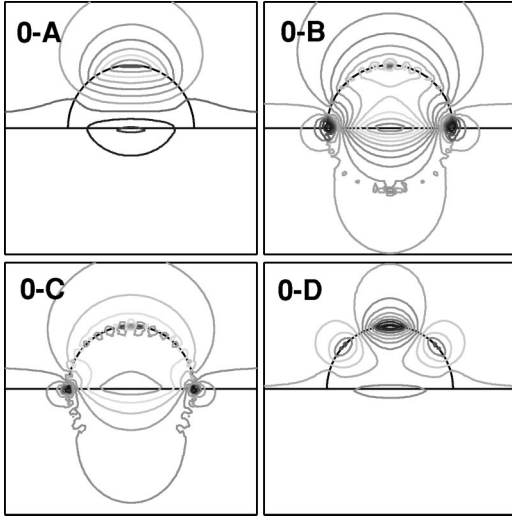


FIG. 3. Maps of potential at order $M=28$ along a plane perpendicular to the substrate ($y=0$) for the four most intense normal ($m=0$) modes (from A to D) for a hemisphere of silver on a dielectric substrate ($\epsilon_2=3$).

All the others modes displayed in Figs. 3 and 4 are of quadrupolar nature. Although these are optically inactive for an isolated sphere, they show up in the present conditions because the breaking of symmetry due to the particle truncation and the presence of the substrate increase drastically their oscillator strengths. Roughly, one order of magnitude is lost between each type of mode: dipolar, quadrupolar, As a consequence the shape of the absorption given by the imaginary part of the polarizability (Fig. 2) is mainly governed by the few first mode and in some situations only by the dipolar ones (0-A,1-A).

C. Substrate-induced depolarization field

When it is brought in contact with a particle, a dielectric substrate creates a depolarization field which perturbs both

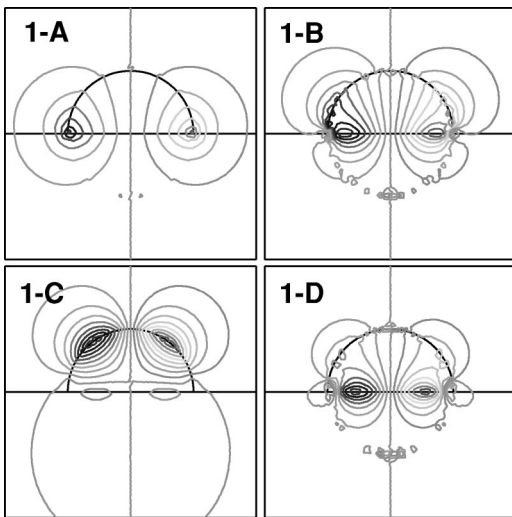


FIG. 4. Same plots as for Fig. 3 for the parallel modes ($m=1$).

the oscillator strength and the energy of each mode. As a trend, the modes represented in Figs. 3 and 4 are redshifted when the real part of the dielectric constant ϵ_2 increases (Fig. 5). This can be explained in the framework of the dipole interaction model by replacing a particle of polarizability α by a dipole at a distance d from the surface. Accounting for the substrate-induced local field on the dipole, the polarizability is renormalized by this depolarization field in the following way:

$$\alpha_{\parallel}^* = \frac{\alpha_{\parallel}}{1 + A\alpha_{\parallel}}, \quad \alpha_{\perp}^* = \frac{\alpha_{\perp}}{1 + 2A\alpha_{\perp}}, \quad (12)$$

where

$$A = \frac{1}{32\pi\epsilon_1 d^3} \frac{\epsilon_1 - \epsilon_2}{\epsilon_1 + \epsilon_2}.$$

Here A characterizes the image dipole strength. Indeed, the frequency of a Lorentz oscillator,

$$\alpha = \frac{F_r}{\omega_r - \omega - i\gamma_r}, \quad (13)$$

is redshifted proportionally to its oscillator strength, since A is negative. One has

$$\alpha_{\parallel}^* = \frac{F_r}{\omega_r - \omega + AF_r - i\gamma_r}, \quad \alpha_{\perp}^* = \frac{F_r}{\omega_r - \omega + 2AF_r - i\gamma_r}. \quad (14)$$

In other words, the image dipole creates a depolarization field which acts in the opposite direction as the force between the electronic gas and the positive background of ions, thus reducing its effective restoring force. However, this model does not end up with a modification either of the oscillator strength (observed in Figs. 3 and 4) or of the broadening. Moreover, the divergence of the dipole interaction when $d \rightarrow 0$ indicates that the high-order coupling must be accounted for.

After a careful analysis, modes can be classified into two categories: those arising from the field singularity at the truncation angle of the supported particle (0-B, 0-C, 1-A, and 1-B), which are mildly perturbed by the substrate, and those due to charges at the particle/substrate interface, which are very sensitive to the contact with the substrate (0-A, 0-D, 1-C, and 1-D). For instance, the oscillator strengths of the modes denoted (0-A) and (0-D) in Fig. 3 and (1-C) in Fig. 4 increase by four orders of magnitude upon increasing ϵ_2 with the substrate. Therefore, because the most intense modes undergo the strongest shifts upon increasing ϵ_2 , the presence of the substrate may help revealing features of higher multipolar order.

However, contact with the substrate also results in a damping of the oscillations through dissipative processes and, consequently, in an increase of the width of the modes (see Fig. 6) with increasing the imaginary part of the dielectric function ϵ_2 . As expected, Fig. 7 demonstrates that the higher the vibrating charge at the interface, the higher is the damping (broadening) of the modes. Thus, as always, an increase of $\text{Re}(\epsilon_2)$ implies an increase of $\text{Im}(\epsilon_2)$, there is an experimental limit in the use of the substrate interaction to isolate multipolar features.

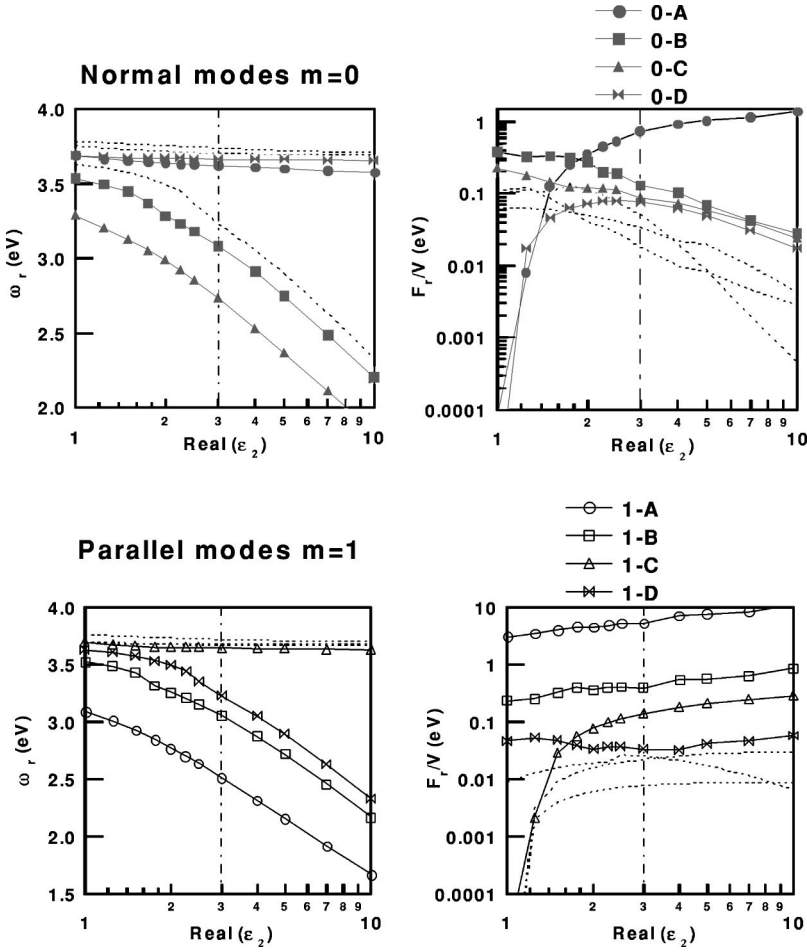


FIG. 5. Influence of the substrate-induced depolarization field on the oscillator strengths and frequencies of the most active modes for a silver hemisphere ($M=20$). The lines with symbols correspond to the (A-B-C-D) modes of Figs. 3 and 4 (vertical dotted line $\epsilon_2=3$). The other dotted lines correspond to less important modes.

D. Particle-particle interactions: A way to shift the resonances

Another important point is how these multipolar modes behave upon interactions between particles. In the framework of the quasistatic approximation, it has been shown that it is sufficient, up to a rather high coverage (50%), to take into account particle interactions only up to dipolar order by

a renormalization of the polarizability in the following way:^{27–31}

$$\alpha_{\perp}^I = \frac{\alpha_{\perp}}{1 - 2\alpha_{\perp}I_{\perp}^{20}}, \quad \alpha_{\parallel}^I = \frac{\alpha_{\parallel}}{1 + \alpha_{\parallel}I_{\parallel}^{20}}. \quad (15)$$

Here, α_{\perp} or α_{\parallel} stands for the polarizabilities of a cluster in interaction with the substrate as calculated from Eqs. (A6) and (A7). The interactions functions I^{20} are defined by:

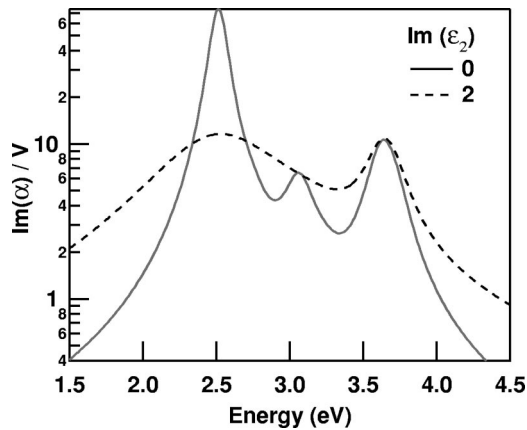


FIG. 6. Effect of the damping in the substrate on the imaginary part of the polarizability [$\text{Re}(\epsilon_2)=3, M=20$]. Note the disappearance of the intermediate quadrupolar feature upon broadening of the structures.

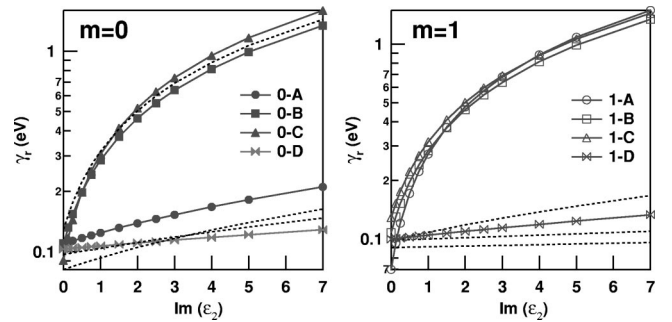


FIG. 7. Influence of the imaginary part of the substrate dielectric constant on the widths of the modes [$M=20, \text{Re}(\epsilon_2)=3$]. The lines with symbols correspond to the four modes seen in Figs. 3 and 4 with the same convention as in Fig. 5.

$$I_{\perp}^{20} = \frac{1}{\sqrt{20\pi\epsilon_1 L^3}} \left[S_{20} - \left(\frac{\epsilon_1 - \epsilon_2}{\epsilon_1 + \epsilon_2} \right) \tilde{S}_{20}^r \right],$$

$$I_{\parallel}^{20} = \frac{1}{\sqrt{20\pi\epsilon_1 L^3}} \left[S_{20} + \left(\frac{\epsilon_1 - \epsilon_2}{\epsilon_1 + \epsilon_2} \right) \tilde{S}_{20}^r \right]. \quad (16)$$

The higher the substrate coupling and the coverage, the larger these I^{20} functions are. The direct S_{20} and \tilde{S}_{20}^r images lattices sums by:

$$S_{20} = \sum_{i \neq 0} \left(\frac{L}{r} \right)^3 Y_2^0(\theta, \phi)|_{\mathbf{r}=\mathbf{R}_i},$$

$$\tilde{S}_{20}^r = \sum_{i \neq 0} \left(\frac{L}{r} \right)^3 Y_2^0(\theta, \phi)|_{\mathbf{r}=\mathbf{R}_i^r}. \quad (17)$$

Here S_{20} describes the interaction with the others direct dipoles placed at $\mathbf{r}=\mathbf{R}_i$ whereas the effect of image dipoles at $\mathbf{r}=\mathbf{R}_i^r$ is included in \tilde{S}_{20}^r . L is the lattice parameter of the dipoles network where are placed the particles. No strong discrepancies were found up to rather high coverage (up to 50%) between regular and random arrays of dipoles.³¹ Notice that the term $i=0$ is excluded as the polarizability α is that of an interacting island. These formulas are valid only for the island case. For the cap particle, one has to invert ϵ_1 and ϵ_2 .

By putting the expression (10) into Eq. (15) and by implicitly making a development to order zero around each mode one finds:

$$\alpha \simeq \sum_r \frac{F_r}{\omega_r^l - \omega - i\gamma_r}, \quad (18)$$

with

$$(\omega_r^l)_{\perp} = (\omega_r)_{\perp} - 2I_{\perp}^{20}(F_r)_{\perp}, \quad (\omega_r^l)_{\parallel} = (\omega_r)_{\parallel} + I_{\parallel}^{20}(F_r)_{\parallel}. \quad (19)$$

These expressions demonstrate that particle-particle interactions only induce a frequency shift of the oscillator, proportional to its strength, but its strength and width remain constant. Parallel and normal modes shifts have opposite sign if the term I^{20} keeps constant over the spectral range which is the case with dielectric substrate in the UV visible. Notice that the negative sign of the I^{20} terms justifies the blueshift and redshift of the $m=0$ and $m=1$ modes, respectively.

V. MULTIPOLAR RESONANCES FOR SILVER ON ALUMINA

The formalism of the surface susceptibilities developed by Bedeaux and Vlieger³²⁻³⁵ allowed us to derive the formulas of differential reflectivity on a nonabsorbing dielectric substrate ϵ_2 :

$$\frac{\Delta R_s}{R_s} = 4 \frac{\omega}{c} \frac{n_1 \cos \theta}{\epsilon_2 - \epsilon_1} \text{Im}(\gamma),$$

$$\frac{\Delta R_p}{R_p} = 4 \frac{\omega}{c} \frac{n_1 \cos \theta}{(\epsilon_2 - \epsilon_1)(\epsilon_1 \sin^2 \theta - \epsilon_2 \cos^2 \theta)} \times \{ (\epsilon_2 - \epsilon_1 \sin^2 \theta) \text{Im}(\gamma) - \epsilon_2^2 \epsilon_1 \sin^2 \theta \text{Im}(\beta) \}, \quad (20)$$

with $\gamma = \rho \alpha_{\parallel}^l$ and $\beta = \rho \alpha_{\perp}^l / (\epsilon^*)^2$ [Eqs. (15)]. $\epsilon^* = \epsilon_1, \epsilon_2$ for an island and a cap, respectively, and θ is the angle of incidence. ρ is the surface density of clusters. Equations (20) demonstrate clearly that the SDR spectra arise from the imaginary part of the particle susceptibilities, i.e., from the absorption. It has to be noticed that the same type of formulas were derived by Bagchi *et al.*³⁶ for the reflectivity of a surface with a nonlocal surface dielectric tensor. By putting the spectral representation, Eq. (A18), into Eqs. (20), as expected, the parallel polarizability determines the SDR spectra in s polarization whereas in p polarization, the normal and parallel modes appear with opposite sign.

For small particles, it was established several years ago that the bulk mean free path of the conduction electrons is increased by the scattering at the surface of the particle. For silver, a classical finite-size correction is often used for s electrons:^{1,6}

$$\epsilon(\omega) = \epsilon_B(\omega) + \frac{\omega_p^2}{\omega^2 + i\omega\tau_B^{-1}} - \frac{\omega_p^2}{\omega^2 + i\omega\tau^{-1}}, \quad (21)$$

where ϵ_B is the bulk dielectric function, $\hbar\omega_p = 9.17$ eV is the plasma frequency of s electrons alone, and $\hbar/\tau_B = 0.018$ eV is the bulk relaxation time. The main effect of such a correction is to modify, quasiuniformly, the width γ_r of the absorption modes. The key point is the energetic position of the modes as the increase of \hbar/τ results in an increase of $\text{Im}(\epsilon_3)$ in the low-energy part of the spectrum.

The present model of a truncated sphere was used to fit the experimental data with a finite-size correction for the silver dielectric constant, Eq. (21). The correction for the relaxation time was

$$\frac{\hbar}{\tau} = \frac{\hbar}{\tau_B} + \frac{v_F}{R}, \quad (22)$$

where $v_F = 0.91$ eV nm is the Fermi velocity and R the particle radius. The particles were placed on an hexagonal lattice. The best agreement with the 4-nm spectrum shown in Fig. 8 was obtained with a radius $R = 6.4$ nm, a density $\rho = 3.2 \times 10^{11}$ part cm⁻², and a truncation parameter $t_r = 0.57$. The obtained thickness $e = 2.8$ nm is a bit lower than the nominal thickness because of the sticking coefficient being lower than 1.³⁷ Here $t_r = 0.57$ leads to an effective contact angle of $\theta_c = 125^\circ$ close to that expected for the expected equilibrium shape. All the features are accounted for by the present model, in particular the shoulder in p polarization. This shoulder is revealed upon the increase of the deposited thickness by the electromagnetic coupling between the growing particles. Indeed, this feature appears when the dispersion with the deposited thickness of the high-energy resonance in p polarization (inset in Fig. 1) changes sign. At the beginning of the growth, the size of the particles is such

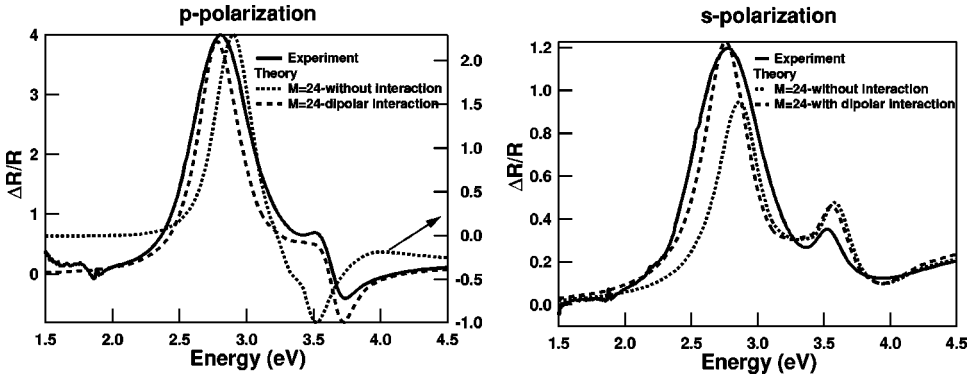


FIG. 8. Comparison between the truncated sphere model at order $M=24$ and the 4-nm SDR spectrum of Fig. 1 in p polarization (left panel) and s polarization (right panel).

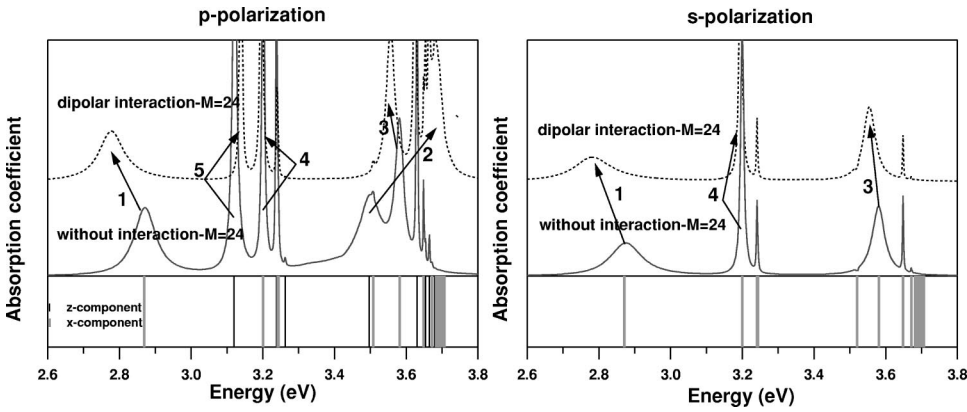


FIG. 9. Computed absorption coefficient at order $M=24$ of the 4-nm layer of $\text{Ag}/\text{Al}_2\text{O}_3(0001)$ by reducing the imaginary part of the metal dielectric constant ($0.01\epsilon_3$). The interparticle coupling up to dipolar order is accounted for in the dotted line plot whereas it is switched off for the solid line plot. The locations of the modes are marked with vertical bars in the lower panel according to their activity.

that the surface plasma resonance is shifted towards blue.^{38–40} This quantum size effect disappears when the ratio surface over volume increases, leading to a redshift in the above-mentioned energy shift. Then a new blueshift shows up because of particle coupling (see Sec. IV D). The interparticle coupling is essential to the appearing of the intermediate shoulder in p polarization whereas in s polarization the peak is present even at the beginning of the growth. To isolate the absorption structures in the simulation, the imaginary part of the silver dielectric constant was drastically reduced to 1% of its value in the absorption coefficient of the layer (Fig. 9). Five main modes are isolated with roughly the correspondence given in Table I with the above mentioned modes.

Obviously, the quadrupolar modes 3-4-5 modify completely the overall shape of the SDR spectra. In p polarization (Fig. 9), the situation is complicated by the fact that all the $m=0, \pm 1$ modes are active and, as demonstrated with Eq. (20), act with opposite signs as shown in Fig. 10 (upper panels). As a consequence, the structures are isolated in experiments only when the particle interaction pushes away the mode frequencies according to their oscillator strengths and

TABLE I. Correspondence with the modes depicted in Figs. 3 and 4 and the isolated structures for silver deposited on alumina. D and Q mean dipole and quadrupole, respectively.

Peaks	1	2	3	4	5
	1-A	0-A	1-C	1-D	0-B
Nature	D_{\parallel}	D_{\perp}	Q_{\parallel}	Q_{\parallel}	Q_{\perp}

to their activity $m=0, \pm 1$ [Eq. (19)]. In s polarization, the $m=0$ modes are inactive and the spectrum is greatly simplified, allowing to appear only the structure 3-4 (Fig. 10, lower panels, and Fig. 1). It is interesting to notice that the spectral decomposition [Eq. (A18)] is unable to describe the optical behavior beyond $E=3.8$ eV. Indeed, the interband $5s-5p$ transitions in bulk silver⁴¹ are not accounted for in this type approach as the absorption is only described in terms of plasmon oscillations which are artificially broadened. Of course, the full solution of the linear system in the Appendix accounts for this phenomenon. This onset of interband transitions appears, like the plasma oscillation, from the early beginning of the growth, implying that the clusters size is sufficient enough to develop the band structure. To completely assess this decomposition, the 4-nm spectrum in s polarization was fitted with three Lorentzians (Fig. 11) as suggested by formula (20). A linear background was subtracted and to get rid of the interband transition the spectral range was limited below 4 eV. The obtained parameters are presented in Table II.

The agreement is fairly good for the peak position. The calculated intensities do not take into account the coupling

TABLE II. Experimental and theoretical values for the 4-nm SDR-spectrum multipolar decomposition.

	Peak 1	Peak 3	Peak 4
Position (eV)	2.75–2.78	3.54–3.55	3.05–3.19
Width (eV)	0.27–0.16	0.10–0.14	0.14–0.17
Intensity (a.u.)	1.04–0.46	0.06–0.16	0.06–0.03

between modes due to the particle interaction [Eqs. (18)] which seems to modify the oscillator strength as seen in Fig. 10. For the quadrupole modes, the order of magnitude for the widths is correct but the dipolar mode is broader than expected, which may be because of a size distribution.

V. CONCLUSION

A formalism of multipolar absorptions has been developed to understand the optical properties of supported nanoparticles. Even if the size of the particle is smaller than the optical wavelength, the nonhomogenous field generated by the image term inside the substrate and the realistic shape of the cluster modify drastically the problem of the absorption of light by allowing the excitation of high-multipolar-order modes. The multipolar expansion of the potential gave the opportunity to derive a spectral representation of the particle polarizability in terms of damped oscillators. The influence of the various parameters on the oscillator strength, width, and frequency has been carefully examined. By taking advantage of the polarization activity and the particle-particle coupling, quadrupolar absorptions were clearly isolated in some experiments of differential reflectivity for silver deposits on oxide substrate.

APPENDIX

Expansion of the potential

The chosen particle shape is that of a truncated sphere of radius R (medium 3) supported on a substrate (medium 2) and embedded in medium 1. The buried part of the sphere is introduced as a different medium (medium 4). The origin of the coordinates system \mathcal{O} is taken at the center of the sphere and the z axis is oriented downwards, pointing into the di-

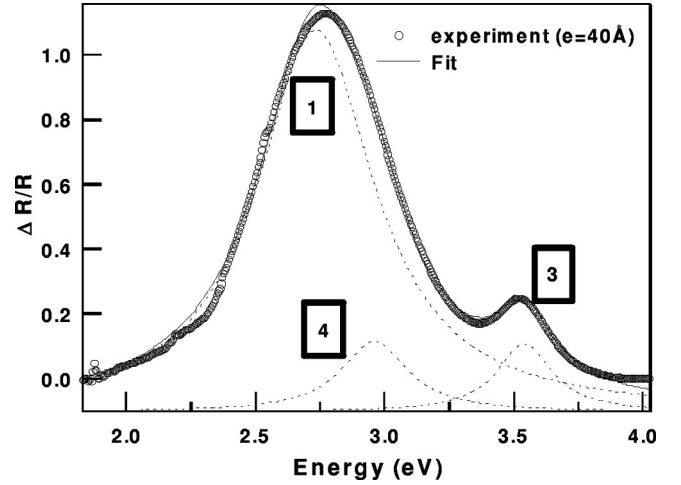


FIG. 11. Fitting of the 4-nm SDR spectrum in s polarization with the three main Lorentzian peaks of Fig. 9. Notice that a linear background was subtracted.

rection of the substrate. The substrate plane is defined through its altitude $z=d$ with $-R \leq d \leq R$ and the image point \mathcal{O}' is introduced as the symmetric point $(0,0,2d)$ with respect to the surface. A point $P(x,y,z)$ is marked by its spherical coordinates (r,θ,ϕ) in the \mathcal{O} system and (ρ,θ_r,ϕ_r) in the \mathcal{O}' system.²⁴ The signed quantity

$$t_r = \frac{d}{R} \quad \text{with} \quad -1 \leq t_r \leq 1 \quad (\text{A1})$$

is introduced as a truncation parameter. $t_r=1$ is a sphere touching the substrate in only one point, and $t_r=0$ corresponds to a hemisphere whereas $t_r=-1$ is associated with a

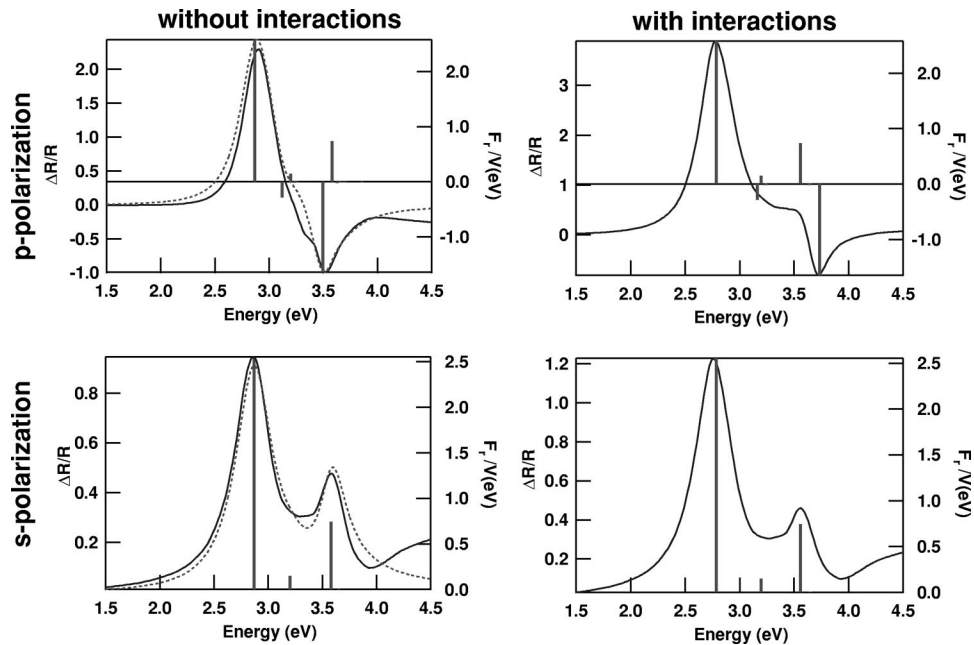


FIG. 10. Calculated SDR spectra for the fitted morphology with the location and integrated intensities of the absorption modes. The curves are computed either directly by solving the linear system, Eq. (A5) (solid line), or by the spectral representation of Eq. (A18) (dotted line) at order $M=24$.

completely buried particle. As a language convention, a $t_r > 0$ particle is called an island while a cap designates a $t_r < 0$ particle. The system is excited by a uniform field \mathbf{E}_0 with polar coordinates (θ_0, ϕ_0) . The dielectric functions of the various media are denoted ϵ_i with $i = 1, 2, 3, 4$ ($\epsilon_4 = \epsilon_2$).

The Laplace equation has been already solved for a positive truncation ratio $t_r \geq 0$ (Refs. 24, 25, 27, and 42) by using spherical multipoles⁴³ $Y_l^m(\theta, \phi)$ (see Ref. 24 for the precise definition) and treating the substrate plane by the charge image technique. For $t_r < 0$, this approach no longer hold. Wind and Vlioger^{27,42} suggested to use a trick consisting of inverting the axis system to derive the cap case $t_r < 0$ from the final formulas of the island one, $t_r > 0$. In this context, Simonsen *et al.*²⁴ allowed the expansion center to freely move on the revolution axis in order to always keep it inside the physical domain. But as the spherical symmetry is lost, the computational burden greatly increased. Even if the final formulas of the Wind-Vlioger *et al.* approach are correct, the underlying expansion of the potential used is not transparent. Here, we give the complete derivation of the potential for $t_r < 0$, in a completely analogous way as for $t_r > 0$:

$$\begin{aligned}\Psi_1(\mathbf{r}) &= \Psi_0(\mathbf{r}) + \sum_{lm}^{l \neq 0} A_{lm}^t r^{-l-1} Y_l^m(\theta, \phi), \\ \Psi_2(\mathbf{r}) &= \Psi_0^t(\mathbf{r}) + \sum_{lm}^{l \neq 0} A_{lm} r^{-l-1} Y_l^m(\theta, \phi) \\ &\quad + \sum_{lm}^{l \neq 0} A_{lm}^r \rho^{-l-1} Y_l^m(\theta^r, \phi^r), \\ \Psi_3(\mathbf{r}) &= \psi_0 + \sum_{lm}^{l \neq 0} B_{lm}^t r^l Y_l^m(\theta, \phi), \\ \Psi_4(\mathbf{r}) &= \psi_0 + \sum_{lm}^{l \neq 0} B_{lm} r^l Y_l^m(\theta, \phi) + \sum_{lm}^{l \neq 0} B_{lm}^r \rho^l Y_l^m(\theta^r, \phi^r).\end{aligned}\tag{A2}$$

$\Psi_0(\mathbf{r})$ and $\Psi_0^t(\mathbf{r})$ (Refs. 24 and 25) are the potentials induced by the uniform incident and transmitted fields, respectively. ψ_0 is a matching constant. In medium 1, the field is transmitted from point \mathcal{O} to the surface, giving rise to the term A_{lm}^t .

The boundary conditions, i.e., continuity of potential and of normal displacement field,^{24,25} are the following at each interface \mathbf{r}_s between media i and j :

$$\Psi_i(\mathbf{r}_s) = \Psi_j(\mathbf{r}_s), \quad \partial_n \Psi_i(\mathbf{r}_s) = \partial_n \Psi_j(\mathbf{r}_s).\tag{A3}$$

These are used to get the unknown multipolar coefficients A_{lm}, B_{lm}, \dots . In comparison to the $t_r > 0$ case, those at the substrate surface are modified in the following way (valid for $t_r < 0$):

$$\begin{aligned}A_{lm}^r &= (-1)^{l+m} \frac{\epsilon_2 - \epsilon_1}{\epsilon_2 + \epsilon_1} A_{lm}, & A_{lm}^t &= \frac{2\epsilon_2}{\epsilon_2 + \epsilon_1} A_{lm}, \\ B_{lm}^r &= (-1)^{l+m} \frac{\epsilon_4 - \epsilon_3}{\epsilon_4 + \epsilon_3} B_{lm}, & B_{lm}^t &= \frac{2\epsilon_4}{\epsilon_4 + \epsilon_3} B_{lm}.\end{aligned}\tag{A4}$$

To get the multipole unknown independent coefficients A_{lm} and B_{lm} , the boundary conditions on the sphere surface are used. The boundary conditions, Eqs. (A3), are projected on a spherical harmonic $Y_l^m(\theta, \phi)$ using the fact that these functions form a complete basis on the sphere surface. This weak formulation of the boundary conditions gives an infinite linear set of equations for the multipolar coefficients for $l = 1, 2, 3, \dots$ and $m = 0, \pm 1$:

$$\begin{aligned}\sum_{l_1=1}^{\infty} C_{ll_1}^m R^{-l_1-2} A_{l_1 m} + \sum_{l_1=1}^{\infty} D_{ll_1}^m R^{l_1-1} B_{l_1 m} &= H_l^m, \\ \sum_{l_1=1}^{\infty} F_{ll_1}^m R^{-l_1-2} A_{l_1 m} + \sum_{l_1=1}^{\infty} G_{ll_1}^m R^{l_1-1} B_{l_1 m} &= J_l^m.\end{aligned}\tag{A5}$$

The equations with the matrix elements for an island or a cap are given hereafter. The right-hand side of this system describes the source field \mathbf{E}_0 while the matrix system represents the geometric and dielectric response function of the island. The potential is fully obtained with the constant term ψ_0 given by the equations containing H_0^0 . Its expression is given in the Appendix. The system, Eqs. (A5), is solved numerically by truncating it at an arbitrary multipole order M . Here M is in principle chosen²⁴ such that the boundary conditions and thus the potential converged with the desired accuracy.

The effective polarizability tensor links the dipole moment \mathbf{p} of the charge distribution and the applied external field \mathbf{E}_0 : $\mathbf{p} = \bar{\bar{\alpha}} \mathbf{E}_0$. Because of the symmetry constraints of the system, only two components of $\bar{\bar{\alpha}}$ parallel and normal to the surface ($\alpha_{\parallel}, \alpha_{\perp}$) are nonzero. The terms in r^{-2} in the multipolar expansion in medium 1 give the far-field dipole behavior with the following relations between the polarizabilities and the multipole coefficients for an island ($t_r > 0$):

$$\begin{aligned}\alpha_{\perp} &= 2\pi\epsilon_1 A_{10} / [\sqrt{\pi/3} E_0 \cos \theta_0], \\ \alpha_{\parallel} &= -4\pi\epsilon_1 A_{11} / [\sqrt{2\pi/3} E_0 \sin \theta_0 \exp(-i\phi_0)].\end{aligned}\tag{A6}$$

In the cap case ($t_r < 0$), the dividing electric field is $(\epsilon_1/\epsilon_2)E_0 \cos \theta_0$ instead of $E_0 \cos \theta_0$ for the z component, whereas the parallel one is kept at $E_0 \sin \theta_0 \exp(-i\phi_0)$, because the direct multipoles are located below the surface. Moreover, ϵ_1 should be replaced by ϵ_2 :

$$\begin{aligned}\alpha_{\perp} &= 2\pi\epsilon_2 A_{10} / [(\epsilon_1/\epsilon_2) \sqrt{\pi/3} E_0 \cos \theta_0], \\ \alpha_{\parallel} &= -4\pi\epsilon_2 A_{11} / [\sqrt{2\pi/3} E_0 \sin \theta_0 \exp(-i\phi_0)].\end{aligned}\tag{A7}$$

Matrix elements and the constant potential ψ_0

The boundary equations (A3) lead after a straightforward algebra to the linear system, Eqs. (A7), whose matrix elements are given by:

$$\begin{aligned}
C_{ll_1}^m &= u_{21} \left(\frac{2\epsilon_1}{\epsilon_1 + \epsilon_2} \right) \delta_{ll_1} - v \left(\frac{\epsilon_1 - \epsilon_2}{\epsilon_1 + \epsilon_2} \right) \\
&\quad \times \zeta_{ll_1}^m \{ Q_{ll_1}^m(t_0) - (-1)^{l_1+m} S_{ll_1}^m(t_0) \}, \\
D_{ll_1}^m &= -u_{43} \left(\frac{2\epsilon_3}{\epsilon_3 + \epsilon_4} \right) \delta_{ll_1} + v \left(\frac{\epsilon_3 - \epsilon_4}{\epsilon_3 + \epsilon_4} \right) \\
&\quad \times \zeta_{ll_1}^m \{ Q_{ll_1}^m(t_0) - (-1)^{l_1+m} T_{ll_1}^m(t_0) \}, \\
F_{ll_1}^m &= - \left(\frac{2\epsilon_1\epsilon_2}{\epsilon_1 + \epsilon_2} \right) (l_1 + 1) \delta_{ll_1} - v u_{21} \epsilon_1 \left(\frac{\epsilon_1 - \epsilon_2}{\epsilon_1 + \epsilon_2} \right) \\
&\quad \times \zeta_{ll_1}^m \left\{ (l_1 + 1) Q_{ll_1}^m(t_0) - (-1)^{l_1+m} \left[\frac{\partial}{\partial t} S_{ll_1}^m(t, t_0) \right]_{t=1} \right\}, \\
G_{ll_1}^m &= - \left(\frac{2\epsilon_3\epsilon_4}{\epsilon_3 + \epsilon_4} \right) l_1 \delta_{ll_1} - v u_{43} \epsilon_3 \left(\frac{\epsilon_3 - \epsilon_4}{\epsilon_3 + \epsilon_4} \right) \\
&\quad \times \zeta_{ll_1}^m \left\{ l_1 Q_{ll_1}^m(t_0) + (-1)^{l_1+m} \left[\frac{\partial}{\partial t} T_{ll_1}^m(t, t_0) \right]_{t=1} \right\}, \tag{A8}
\end{aligned}$$

with $t_0 = |t_r|$, $u_{21} = u_{43} = v = 1$ for an island, and $u_{21} = \epsilon_2/\epsilon_1$, $u_{43} = \epsilon_4/\epsilon_3$, $v = (-1)^{l_1+1}$ for a cap. Here the following notation has been introduced:

$$\zeta_{ll_1}^m = \frac{1}{2} \left[\frac{(2l+1)(2l_1+1)(l-m)!(l_1-m)!}{(l+m)!(l_1+m)!} \right]^{1/2}. \tag{A9}$$

In the previous system, the $Q_{ll_1}^m$ are defined by the integrals

$$Q_{ll_1}^m(t_0) = \int_{-1}^{t_0} P_l^m(x) P_{l_1}^m(x) dx. \tag{A10}$$

The matrices $S_{ll_1}^m(t_0)$ and $T_{ll_1}^m(t_0)$ are defined by:

$$S_{ll_1}^m(t_0) = [S_{ll_1}^m(t, t_0)]_{t=1}, \quad T_{ll_1}^m(t_0) = [T_{ll_1}^m(t, t_0)]_{t=1}, \tag{A11}$$

where

$$\begin{aligned}
S_{ll_1}^m(t, t_0) &= \int_{-1}^{t_0} P_l^m(x) P_{l_1}^m([tx - 2t_0]) [t^2 - 4t_0tx + 4t_0^2]^{-1/2} \\
&\quad \times (t^2 - 4t_0tx + 4t_0^2)^{-(l_1+1)/2} dx, \tag{A12}
\end{aligned}$$

$$\begin{aligned}
T_{ll_1}^m(t, t_0) &= \int_{-1}^{t_0} P_l^m(x) P_{l_1}^m([tx - 2t_0]) [t^2 - 4t_0tx + 4t_0^2]^{-1/2} \\
&\quad \times (t^2 - 4t_0tx + 4t_0^2)^{l_1/2} dx, \tag{A13}
\end{aligned}$$

with

$$t \equiv \frac{r}{R}, \quad x \equiv \cos \theta. \tag{A14}$$

One can recognize the Legendre functions $P_l^m(x)$ defined in Refs. 24 and 25. The source field is given by:

$$\begin{aligned}
H_l^0 &= \sqrt{4\pi/3} E_0 \cos \theta_0 \left\{ u_{21} \frac{\epsilon_1}{\epsilon_2} \delta_{l1} + v \left(\frac{\epsilon_1 - \epsilon_2}{\epsilon_2} \right) \right. \\
&\quad \left. \times [\sqrt{3} t_0 \zeta_{l0}^0 Q_{l0}^0(t_0) - \zeta_{l1}^0 Q_{l1}^0(t_0)] \right\}, \\
J_l^0 &= \sqrt{4\pi/3} E_0 \cos \theta_0 \epsilon_1 \delta_{l1}, \\
H_l^1 &= -\sqrt{2\pi/3} E_0 \sin \theta_0 \exp(-i\phi_0) \delta_{l1}, \\
J_l^1 &= -\sqrt{2\pi/3} E_0 \sin \theta_0 \exp(-i\phi_0) [u_{12} \epsilon_2 \delta_{l1} \\
&\quad + v(\epsilon_1 - \epsilon_2) \zeta_{l1}^1 Q_{l1}^1(t_0)], \tag{A15}
\end{aligned}$$

with $v = 1$ and $(-1)^{l+2}$ for an island and a cap, respectively. To conclude the constant term ψ_0 [Eq. (A2)] which permits one to match the potential inside and outside the sphere is found in terms of the multipole coefficients thanks to the $l = 0$ equation of the linear system:

$$\begin{aligned}
\psi_0 &= R \left(\frac{\epsilon_1}{\epsilon_2} - 1 \right) \left\{ \frac{1}{\sqrt{3}} \zeta_{00}^0 Q_{00}^0(t_0) + t_0 [p - \zeta_{00}^0 Q_{00}^0(t_0)] \right\} \\
&\quad \times E_0 \cos \theta_0 - \frac{1}{2\sqrt{\pi}} \sum_{l=1}^{\infty} A_{l0} R^{-l-1} q \left(\frac{\epsilon_1 - \epsilon_2}{\epsilon_1 + \epsilon_2} \right) \\
&\quad \times \zeta_{0l}^0 [Q_{0l}^0(t_0) - (-1)^l S_{0l}^0(t_0)] + \frac{1}{2\sqrt{\pi}} \\
&\quad \times \sum_{l=1}^{\infty} B_{l0} R^l q \left(\frac{\epsilon_3 - \epsilon_4}{\epsilon_3 + \epsilon_4} \right) \zeta_{0l}^0 [Q_{0l}^0(t_0) - (-1)^l T_{0l}^0(t_0)], \tag{A16}
\end{aligned}$$

with $p = q = 1$ for an island and $p = 0$, $q = (-1)^{l+1}$ for a cap.

Spectral representation of the polarizability

Being decomposed in a sum of damped Lorentz oscillators, in the limit $\omega \rightarrow \omega_r$, the polarizability is written in Eq. (10) in a local Kramers-Heisenberg form. In the limit $\kappa = 0$, the system behaves as a sum of undamped oscillators with Dirac absorptions:

$$\alpha = \sum_r F_r \mathcal{P} \left(\frac{1}{\omega_r - \omega} \right) + i\pi \sum_r F_r \delta(\omega - \omega_r), \tag{A17}$$

where \mathcal{P} is the principal part. Of course, in the form (10), the polarizability does not fulfill the Kramers-Kronig relation⁴⁴ as it results from a local development around each mode. It is possible to artificially impose this condition by writing

$$\alpha = \sum_r \frac{2\omega_r F_r}{\omega_r^2 - \omega^2 - i2\omega\gamma_r} + \alpha_0^{KK}(\omega, \kappa). \tag{A18}$$

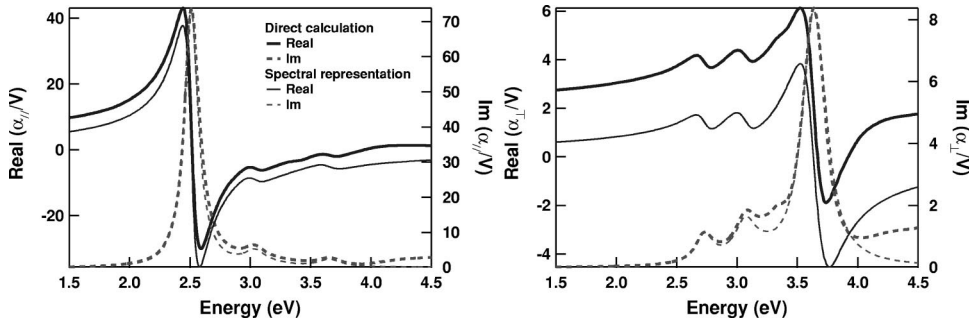


FIG. 12. Comparison between reduced polarizabilities computed directly by solving Eq. (3) (bold curves) or with the spectral representation [sum in Eq. (10)] ($\kappa=1$) (thin curves) for a hemisphere ($t_r=0$) of silver on a substrate with a dielectric constant $\epsilon_2=3$ ($M=24$).

In this approach, the modes are supposed to be uncoupled by the fact that one can choose arbitrary small damping κ and deviation from the resonant point ω_r . This model gives only an estimate of the broadening to first order in κ . Upon approaching the limit $\kappa=1$, the interactions between modes can greatly modify the widths and the oscillator strengths in such a way that the notion itself of eigenmodes loses its meaning. However, polarizability curves computed by solving exactly the system, Eqs. (3), compare quite well with absorptions curves calculated by taking $\kappa=1$. An example for the polarizabilities of a hemisphere of silver is given in Fig. 12. The graph in Fig. 12 shows that the main difference [term $\alpha_0(\omega, \kappa)$ in Eq. (10)] comes from a mainly constant shift of the real part of the polarizability. The consequence on the optical properties of islands layers is negligible since they depend mainly on the imaginary part of the polarizabilities. Notice that the spectral representation is not able to describe the increase of absorption beyond $E=3.8$ eV; this phenomenon is linked to interband transitions in silver and not to collective damped oscillations of the electric charge.

A careful analysis of the matrix, Eqs. (A5), shows that its determinant is a rational function of order M in the particle dielectric constant ϵ_3 . Thus, for a substrate whose dielectric constant presents a small dependence on frequency, the maximum number of modes is given by the size of multipole

lar basis M . Obviously, their optical activity F_r depends on the dielectric constants of the materials and on the system geometry.

Numerical implementation of the oscillator strength and broadening

The Legendre polynomials $P_l^m(x)$ are computed through stable recurrence relations.^{45,46} The integrals $Q_{ll_1}^m(t_r)$, $S_{ll_1}^m(t_r)$, $T_{ll_1}^m(t_r)$ [Eqs. (A10)–(A13)] are computed by numerical integration with the algorithm of Piessens *et al.*⁴⁷ which handles well the strong oscillating behavior of the Legendre polynomials. However, recurrence relations for these integrals derived in Ref. 27 have shown that they are regular functions (polynomials) of the truncation parameter. For finding the multipolar absorptions peaks, first the roots of the determinant of the matrix system $\mathcal{M}(\omega, 0)$, Eq. (A5), are bracketed by dichotomy. The matrix determinant is computed by the LAPACK LU-decomposition scheme.⁴⁸ The associated left $X(\omega, 0)$ and right $Y(\omega, 0)$ eigenvectors are then found by an inverse iteration process.⁴⁵ The development of terms in $(\epsilon_i - \epsilon_j)/(\epsilon_i + \epsilon_j)$ around $\omega = \omega_r$ and $\kappa=0$ gives the derivative matrices $\partial\mathcal{M}/\partial\omega|_{\omega_r, \kappa=0}$ and $\partial\mathcal{M}/\partial\omega|_{\omega_r, \kappa=0}$. Thus using the formulas (11), one is able to compute the oscillator strength F_r and broadening γ_r for parallel ($m = \pm 1$) and perpendicular ($m = 0$) modes.

*Electronic address: Lazzari@drfmc.ceng.cea.fr

†Electronic address: Stephane.Roux@saint-gobain.com

‡Electronic address: Ingve.Simonsen@phys.ntnu.no

§Electronic address: Jacques.Jupille@saint-gobain.com

||Electronic address: bedeaux@chem.leidenuniv.nl

¹U. Kreibig and M. Vollmer, *Optical Properties of Metal Clusters* (Springer, Berlin, 1995), Vol. 25.

²J.C. Maxwell Garnett, *Philos. Trans. R. Soc. London, Ser. A* **230**, 385 (1904).

³G. Mie, *Ann. Phys. (Leipzig)* **25**, 377 (1908).

⁴U. Kreibig, B. Schmitz, and H.D. Breuer, *Phys. Rev. B* **36**, 5027 (1987).

⁵A. Lebedev, O. Stenzel, M. Quinten, A. Stendal, Röder, Schreiber, and Zahn D.R.T., *J. Opt. A, Pure Appl. Opt.* **1**, 573 (1999).

⁶H. Hövel, S. Fritz, A. Hilger, U. Kreibig, and M. Vollmer, *Phys. Rev. B* **48**, 18 178 (1993).

⁷B.N.J. Persson, *Surf. Sci.* **281**, 153 (1993).

⁸M. C. Desjonquères and D. Spanjaard, *Concepts in Surface Physics* (Springer-Verlag, Berlin, 1993).

⁹R. Fuchs, *Phys. Rev. B* **11**, 1732 (1975).

¹⁰R. Ruppin, *Surf. Sci.* **127**, 108 (1983).

¹¹C.E. Román-Velázquez, C. Noguez, and R.G. Barrera, *Phys. Rev. B* **61**, 10 427 (2000).

¹²C. Beita, Y. Borensztein, R. Lazzari, J. Nieto, and R.G. Barrera, *Phys. Rev. B* **60**, 6018 (1999).

¹³R. Chauvaux and A. Meesen, *Thin Solid Films* **62**, 125 (1979).

¹⁴T. Yamaguchi, S. Yoshida, and A. Kinbara, *Thin Solid Films* **18**, 63 (1973).

¹⁵T. Yamaguchi, S. Yoshida, and A. Kinbara, *Thin Solid Films* **21**, 173 (1974).

¹⁶T. Wenzel, J. Bosbach, F. Stietz, and F. Träger, *Surf. Sci.* **432**, 257 (1999).

¹⁷V. Coustet and J. Jupille, *Nuovo Cimento D* **19**, 1657 (1997).

¹⁸T. Brandt, W. Hoheisel, A. Iline, F. Stietz, and F. Träger, *Appl. Phys. B: Lasers Opt.* **65**, 793 (1997).

¹⁹A. Iline, M. Simon, F. Stietz, and F. Träger, *Appl. Organomet. Chem.* **12**, 353 (1998).

²⁰A. Iline, M. Simon, F. Stietz, and F. Träger, *Surf. Sci.* **436**, 51 (1999).

- ²¹U. Kreibig, M. Gartz, and A. Hilger, *Berichte der Bunsengesellschaft für Physikalische Chemie* **101**, 1593 (1997).
- ²²T.C. Campbell, *Surf. Sci. Rep.* **27**, 1 (1997).
- ²³C. Henry, *Surf. Sci. Rep.* **31**, 231 (1998).
- ²⁴I. Simonsen, R. Lazzari, J. Jupille, and S. Roux, *Phys. Rev. B* **61**, 7722 (2000).
- ²⁵R. Lazzari, I. Simonsen, D. Bedeaux, J. Vlieger, and J. Jupille, *Eur. Phys. J. B* **24**, 267 (2001).
- ²⁶E. D. Palik, *Handbook of Optical Constants of Solids* (Academic, Orlando, 1985), Vols. 1 and 2.
- ²⁷M.M. Wind and J. Vlieger, *Physica A* **143**, 164 (1987).
- ²⁸J. Vlieger and D. Bedeaux, *Thin Solid Films* **69**, 107 (1980).
- ²⁹D. Bedeaux and J. Vlieger, *Optical Properties of Surfaces* (Imperial College Press, London, 2001).
- ³⁰R.G. Barrera, M. del Castillo-Mussot, and G. Monsivais, *Phys. Rev. B* **43**, 13 819 (1991).
- ³¹M.T. Haarmans and D. Bedeaux, *Thin Solid Films* **224**, 117 (1993).
- ³²D. Bedeaux and J. Vlieger, *Physica A* **67**, 55 (1973).
- ³³D. Bedeaux and J. Vlieger, *Physica (Amsterdam)* **73**, 287 (1973).
- ³⁴D. Bedeaux and J. Vlieger, *Physica A* **82**, 221 (1976).
- ³⁵M.M. Wind and J. Vlieger, *Physica A* **125**, 75 (1984).
- ³⁶A. Bagchi, R.G. Barrera, and R. Del Sole, *Phys. Rev. B* **20**, 4824 (1979).
- ³⁷D.G. Van Campen and J. Hrbek, *J. Phys. Chem. B* **99**, 16389 (1995).
- ³⁸A. Liebsch, *Phys. Rev. B* **48**, 11 317 (1993).
- ³⁹J. Tiggesbäumker, L. Köller, H. Meiwes-Broer, and A. Liebsch, *Phys. Rev. B* **48**, R1749 (1993).
- ⁴⁰Y. Borensztein and D. André, *Phys. Rev. B* **33**, 2828 (1986).
- ⁴¹M.M. Dujardin and M.L. Theye, *J. Phys. Chem. Solids* **32**, 2033 (1971).
- ⁴²M.M. Wind and J. Vlieger, *Physica A* **141**, 33 (1987).
- ⁴³J. D. Jackson, *Classical Electrodynamics* (Wiley, New York, 1975).
- ⁴⁴C. F. Bohren and D. R. Huffman, *Absorption and Scattering of Light by Small Particles* (Wiley, New York, 1983).
- ⁴⁵W. H. Press, S. A. Teukolsky, W. T. Vetterling, and B. P. Flannery, *Numerical Recipes in Fortran* (Cambridge University Press, Cambridge, England, 1992).
- ⁴⁶P. M. Morse and H. Feshbach, *Methods of Theoretical Physics* (McGraw-Hill, New York, 1953).
- ⁴⁷R. Piessens, E. deDoncker Kapenga, C. Uberhuber, and D. Kahaner, *Quadpack: a Subroutine Package for Automatic Integration*, Series in Computational Mathematics Vol. 1 (Springer, Berlin, 1983).
- ⁴⁸E. Anderson, Z. Zai, C. Bischoff, J. Demmel, J. Dongarra, J. Du Croz, A. Greenbaum, S. Hemmarling, A. McKenney, S. Ostrouchov, and D. Sorensen, *Lapack User's Guide* (SIAM, Philadelphia, 1999).